

Article

# Antibacterial and Tribological Performance of Carbonitride Coatings Doped with W, Ti, Zr, or Cr Deposited on AISI 316L Stainless Steel

Sun-Hui Yao <sup>1,\*</sup>, Yen-Liang Su <sup>2</sup> and Yu-Cheng Lai <sup>2</sup>

<sup>1</sup> Chang Jung Christian University, No. 1 Changda Road, Tainan 71101, Taiwan

<sup>2</sup> Department of Mechanical Engineering, National Cheng Kung University, No. 1 University Road, Tainan 70101, Taiwan; suy1@mail.ncku.edu.tw (Y.L.S.); n16054784@mail.ncku.edu.tw (Y.C.L.)

\* Correspondence: shyao0954@gmail.com; Tel.: +886-6-278-5123 (ext. 2226)

Received: 30 August 2017; Accepted: 12 October 2017; Published: 17 October 2017

**Abstract:** Carbonitride (CN<sub>x</sub>) coatings have existed for several decades but are not well understood. Related studies have indicated that CN<sub>x</sub> coatings exhibit behaviors comparable to diamond-like carbon (DLC) coatings. Metal-doped CN<sub>x</sub> coatings are expected to show superior performance to single CN<sub>x</sub> coatings. In this study, a CN<sub>x</sub> coating and a group of CN<sub>x</sub> coatings with 6 at. % metal doping (W, Ti, Zr, or Cr) were prepared on biograde AISI 316L stainless steel (SS316L) substrates, and they were then characterized and studied for antibacterial and wear performance. The microstructure, constituent phase, nanohardness, adhesion, surface roughness, and contact angle were evaluated. The antimicrobial test used *Staphylococcus aureus* and followed the Japanese Industrial Standard JIS Z 2801:2010. Finally, the wear behavior was assessed. The results showed that the CN<sub>x</sub> coating was a composite of amorphous CN<sub>x</sub> and amorphous C structures. The metal doping caused crystalline metal carbides/nitrides to form in the CN<sub>x</sub> coatings, which weakened their overall integrity. All the coatings showed antimicrobial ability for the SS316L samples. The CN<sub>x</sub>-Zr coating, the surface of which had the highest hydrophilicity, produced the best antibacterial performance. However, the CN<sub>x</sub>-Zr coating showed lower wear resistance than the CN<sub>x</sub>-W and CN<sub>x</sub>-Ti coatings. The CN<sub>x</sub>-Ti coating with a highly hydrophilic surface exhibited the lowest antibacterial ability.

**Keywords:** carbon-nitride; metal doping; antibacterial performance; wear behavior

## 1. Introduction

Considering a coating with antibacterial ability, the first candidate would be Ag-containing coating since Ag is a well-known antibacterial element. For example, the silver nanoclusters-silica composite coating with 0.4 at. % Ag showed antibacterial ability and improved bacterial anti-adhesion performance [1]. Another study on a magnetron-sputtered Zr-Cu-Ag composite coating found it showed good mechanical performance, high chemical inertness, and good antimicrobial ability [2].

In the literature, one can find some, but not much, researchers have endeavored to study the sputtered coatings against bacteria. Groessner-Schreiber et al. [3,4] found that the microflora and *Streptococcus* adhesion can be reduced by TiN and ZrN coatings. A study by Huang et al. [5] proved that the TaN coating possessed antibacterial ability against *Staphylococcus aureus* (*S. aureus*), with a conclusion due to the TaN coating being with high hydrophobic surface. In a study by Julius Andrew et al. [6], the magnetron-sputtered TiO<sub>2</sub> coating on PMMA material was studied, which exhibited antibacterial efficiency reaching 70% and a large decrease in the contact angle from 33–66 degrees to 5–30 degrees.

Few studies have been conducted on applying carbon-based coatings against microbes; those which have were limited to diamond-like carbon (DLC) related coatings. Marciano et al. [7]

evaluated the antibacterial ability of DLC coatings using *S. aureus*, *Escherichia coli* (*E. coli*), *Pseudomonas aeruginosa* (*P. aeruginosa*), and *Salmonella*. They found that a DLC coating with an H content of 22 at. % and an intensity ratio of D/G peaks (ID/IG) of 1.23 (detected by Raman spectroscopy) reduced bacterial activity by 25–55% compared with an uncoated sample, depending on the type of bacteria used. Zhou et al. [8] prepared DLC and hydrogenated DLC coatings on SS316L substrates and evaluated their antibacterial ability using *E. coli*. Compared with the uncoated sample, the DLC and hydrogenated DLC coatings reduced the viable bacteria to 15% and 33%, respectively. Studies on carbon-based coatings have demonstrated that surface properties are another factor affecting the adhesion of bacteria [9–11]. Ishihara et al. [12] prepared DLC coatings using a radio frequency magnetron sputtering system and evaluated the effect of the hydrophilicity of coating surfaces on the bacterial retention. The results indicated that the higher the hydrophilicity was, the less the bacteria were retained.

In notable research by Liu and Cohen [13], carbonitride (CN<sub>x</sub>) coatings were found to exhibit hardness comparable to diamonds, particularly when involving covalent  $\beta$ -C<sub>3</sub>N<sub>4</sub> bonding structures. Over the past 30 years, a few studies have been performed on CN<sub>x</sub>. Some results indicated that CN<sub>x</sub> coatings exhibited low friction, high adhesion, and high wear and corrosion resistance. Wäsche et al. found that among evaluated samples, a CN<sub>x</sub> coating showed the highest hardness under deposition conditions with a N/Ar ratio of 0.2 [14]. Takadom et al. determined [15] that a CN<sub>x</sub> coating displayed higher wear resistance than a DLC coating. The same result has been obtained by Park et al. [16] and Camero et al. [17]. The CN<sub>x</sub> coatings, under deposition conditions with N/Ar ratios of 0.25–0.50, possessed the highest content of sp<sup>3</sup> bonding and exhibited the highest wear resistance of their samples.

Other studies have found that the properties of CN<sub>x</sub> coatings, such as hardness, corrosive resistance, antioxidation, and wear resistance, can be enhanced by metal doping [18–21].

Lai et al. [22] grew a series of CN<sub>x</sub>/amorphous C-Zr<sub>0.55–0.60</sub> (a-C) coatings on biograde Ti samples. They found that the coatings showed high biocompatibility and good antibacterial performance when the C content was higher than 12.7 at. %. Huang et al. [23] prepared CN<sub>x</sub> coatings doped with Ti and Zr and evaluated the bacterial viability by using *S. aureus* and *Aggrigatebacter Actinomycetemcomitans*; the results revealed that bacterial viability levels of 21% and 36%, respectively, were obtained. Moreover, the coatings showed high biocompatibility with human fibroblasts. Considerably more studies have been conducted on mechanical properties than on antimicrobial performance.

Hosokawa et al. [24] prepared Ti-doped CN<sub>x</sub> (CN<sub>x</sub>-Ti) coatings on drills by using the magnetron sputtering method and conducting drilling tests. They revealed that the life of the CN<sub>x</sub>-Ti-coated drills was three times that of TiN-coated drills and that the flank wear decreased significantly as well. Kuptsov et al. [25] studied CN<sub>x</sub>-Ti coatings and found that corrosive resistance was improved by the formation of a surface TiO<sub>2</sub> layer. The same mechanism was also found to achieve improvements in wear resistance at 300 °C [26].

In an identical study by Polcara et al. [26], Cr-doped CN<sub>x</sub> (CN<sub>x</sub>-Cr) coatings were prepared and evaluated using an elevated-temperature wear tester. The results showed that at 700 °C, the CN<sub>x</sub>-Cr coatings displayed a friction coefficient close to that at ambient temperature, due to minor variation in wear behavior between the two conditions.

In a study on a series of Zr-doped CN<sub>x</sub> (CN<sub>x</sub>-Zr) coatings, the coatings with 34.3 at. % Zr and a C/N ratio of 0.9 showed a hardness of  $22.8 \pm 1.1$  GPa, low friction, and high adhesion [27]. Wang et al. [28] found that deposition temperature influenced the properties of a CN<sub>x</sub>-Zr coating. As the deposition temperature increased, the mechanical properties improved. At a deposition temperature of 400 °C, the coating showed a hardness of  $32.0 \pm 0.3$  GPa, good adhesion, and a favorable resilience coefficient. Grigore et al. [29] prepared CN<sub>x</sub>-Zr coatings using the magnetron sputtering method. Of the samples, the CN<sub>x</sub>-Zr coating showed the highest hardness (HV 3600) with a Zr content of 52 at. % under deposition of a N/Ar ratio of 0.1125, and that exhibited the highest wear resistance with a Zr content of 54.1 at. % under deposition of a N/Ar ratio of 0.0625. Yao et al. [30] prepared a series of CN<sub>x</sub>-Zr coatings with different N content levels and found that the coating with a Zr content

of 48.7 at. % under deposition of a N/Ar ratio of 0.2 displayed the best wear resistance and highest hardness (HK 1600).

Ospina et al. [31] evaluated the mechanical properties and wear performance of W-doped CN<sub>x</sub> (CN<sub>x</sub>-W) coatings prepared using the pulse arc deposition method. The results indicated that the critical load (*L<sub>c</sub>*) and hardness increased, and the friction coefficient decreased to 0.35 from 0.7, as compared with a single W coating. Chen et al. [32] prepared CN<sub>x</sub>-W and WN<sub>x</sub> coatings and compared their wear behavior. The wear rates for the CN<sub>x</sub>-W and WN<sub>x</sub> coatings were  $3 \times 10^{-8}$  and  $6 \times 10^{-8}$  mm<sup>3</sup>/Nm, respectively. A large improvement in wear resistance was produced by the CN<sub>x</sub>-W coating.

Numerous studies have been conducted on DLC coatings involving various topics. Of these, only a few have discussed antibacterial activity and biocompatibility. Until now, according to our review of the literature, no data have been published concerning CN<sub>x</sub> coatings. In this study, we prepared CN<sub>x</sub> and 6 at. % metal-doped CN<sub>x</sub> coatings on SS316L substrates by using an industrial-scale four-target closed-field unbalanced DC magnetron sputtering system. The metals used were W, Ti, Zr, and Cr. The samples were characterized and evaluated for antibacterial and wear performance. This study was a trial of growing CN<sub>x</sub> and metal-doped CN<sub>x</sub> coatings on SS316L steel; their characteristics and possible applications against bacteria and against wear were investigated.

## 2. Experimental Details

### 2.1. Analysis Equipment

A scanning electron microscope (E-SEM Quanta 400F, FEI, Hillsboro, OR, USA) equipped with an electron dispersive X-ray system was used. A glow discharge spectrometer (GDS-750 QDP, LECO, Saint Joseph, MI, USA) was applied to determine the coating thickness. A glancing-angle X-ray diffractometer (D/MAX2500, Rigaku, Tokyo, Japan) was used, setting Cu K $\alpha$  radiation at 40 kV and 100 mA with a glancing angle of 4°. An X-ray photoelectron spectroscope (PHI 1600 ESCA, Perkin-Elmer Co., Waltham, MA, USA) was used, employing non-monochromatized Mg K $\alpha$  radiation. An X-ray photon spectroscopy (XPS) system was applied with 3 kV Ar ions to sputter the surface oxide layer and examine the chemical composition of the coatings. Spectra ranging from 0 to 1000 eV were recorded for each sample, followed by high-resolution spectra over different elemental peaks, from which the composition was calculated. The spectral ranges at  $287 \pm 7$ ,  $400 \pm 9$ ,  $184 \pm 10$ ,  $582 \pm 13$ ,  $460 \pm 10$ , and  $36 \pm 10$  eV corresponded to the binding energies of C1s, N1s, Zr3d, Cr2p, Ti2p, and W4f, respectively. Curve fitting was performed after a Shirley background subtraction by a Gaussian fitting [33]. Energy calibration was conducted with reference to the Au 4f<sub>7/2</sub> peak at 83.8 eV. A Raman spectrometer (HR 800 Micro PL, Horiba, Kyoto, Japan) employing a He-Ne laser and Peltier-cooled Princeton CCD camera was used. Two peaks were observed in the Raman analyses result, indicating carbon structures corresponding to a D peak at approximately 1363 cm<sup>-1</sup> and a G peak at approximately 1560 cm<sup>-1</sup>. A nanoindentation system (LBI Nanoindenter, UNAT-M, Dresden, Germany) was used at an applied load of 10 mN. Adhesion was evaluated using a scratch tester with an applied load that increased from 0 to 100 N at a rate of 10 N/mm. A critical load (*L<sub>c</sub>*) was obtained.

### 2.2. Coatings

The coatings were prepared using a closed-field unbalanced DC magnetron sputtering system (CFUBMS KD-550U, MIRDC, Kaohsiung, Taiwan), which features four vertical orthogonally-mounted magnetron cathodes surrounding a rotational substrate holder. The dimensions of a target were 437.3 mm  $\times$  178.2 mm  $\times$  10.2 mm.

Biograde SS316L was used as the substrate material. Two types of samples, block and plate, were used. The block had dimensions of 24 mm  $\times$  8 mm (diameter  $\times$  thickness) and the plate of 16 mm  $\times$  16 mm  $\times$  1 mm. The plate sample was used in the antimicrobial test. The substrate surface to be evaluated was polished to a surface roughness Ra < 60 nm.

The standard sample preparation procedure for physical vapor deposition (PVD) was used. After the samples were loaded, the chamber was pumped down to  $2 \times 10^{-5}$  Torr. The main Ar gas and minor H<sub>2</sub> gas were introduced. The H ions were used to maintain the chamber temperature. The Ar ions were used to perform the bombardment conditioning (30 min). The Ar gas flow rate was increased at a steady rate until it reached 25 sccm (corresponding to  $3 \times 10^{-3}$  Torr) at the end of the bombardment process and was then maintained for the subsequent coating.

In this study, CN<sub>x</sub>, CN<sub>x</sub>-W, CN<sub>x</sub>-Ti, CN<sub>x</sub>-Zr, and CN<sub>x</sub>-Cr coatings were prepared. For growth of metal-doped CN<sub>x</sub> coatings, four targets were used, with two carbon targets next to each other and two metal targets in the chamber. The metal targets were the doping material and were also used to prepare an effective interface. For example, in the case of the CN<sub>x</sub>-Ti coating, two Ti and two carbon targets were used. The Ti interlayer was prepared first under a condition of 1 A current for one Ti target for 10 min. The TiC gradual layer was then prepared under conditions of 1 A and 3 A currents for one Ti and two C targets, respectively, for 6 min. Finally, the main CN<sub>x</sub>-Ti coating was prepared under conditions of 1 A and 3 A currents for two Ti and two C targets, respectively, and a N<sub>2</sub> gas flow rate of 6 sccm for 120 min. Identical processes were used to grow the CN<sub>x</sub>-Zr and CN<sub>x</sub>-Cr coatings by using Zr and Cr targets, respectively. The coating procedure for the CN<sub>x</sub>-W coating involved some modification. From long-term experience, we know that the use of a W interface layer leads to poor quality of adhesion for the subsequent main coating. Thus, to grow the CN<sub>x</sub>-W coating, two C targets, one Ti target, and one W target were used. The Ti interface was prepared first at a Ti target using a 1 A current for 10 min., and then the TiC gradual layer was prepared under conditions of 1 A and 2 A currents for one Ti and two C targets, respectively, for 6 min. Finally, the main CN<sub>x</sub>-W coating was prepared under conditions of 0.6 A and 3 A currents for one W and two C targets, respectively, and a N<sub>2</sub> gas flow rate of 6 sccm for 120 min. The aforementioned conditions were set on the basis of repeated tests and trials for the different types of coatings. With these procedures, the overall thickness of the coatings was approximately 2 μm, as determined using glow discharge optical spectroscopy. The amount of doped metal was well controlled at 6–7 at. %, as determined using XPS. The data are listed in Table 1. For growth of the CN<sub>x</sub> coating, one Ti and two carbon targets were used. The Ti interface was prepared first, then the TiC gradual layer, and finally the main CN<sub>x</sub> coating, using the same condition for the CN<sub>x</sub>-Ti coating, with 0 A for the Ti target.

**Table 1.** Composition and thickness of CN<sub>x</sub> and 6 at. % metal-doped CN<sub>x</sub> coatings.

| Samples             | Composition (at. %) |    |    | Coating Thickness (μm) |
|---------------------|---------------------|----|----|------------------------|
|                     | Me                  | C  | N  |                        |
| CN <sub>x</sub>     | -                   | 68 | 32 | 2.0                    |
| CN <sub>x</sub> -W  | 6                   | 60 | 34 | 2.1                    |
| CN <sub>x</sub> -Ti | 6                   | 58 | 36 | 1.6                    |
| CN <sub>x</sub> -Zr | 7                   | 62 | 31 | 1.8                    |
| CN <sub>x</sub> -Cr | 6                   | 58 | 36 | 1.9                    |

### 2.3. Hydrophilicity Test

The hydrophilicity of the surface of the samples was evaluated by measuring the static contact angles using a contact-angle analyzer (FTA-1000B, Portsmouth, VA, USA). Each specimen was alternately washed in ethanol and deionized water in an ultrasonic cleaner for 30 min and then dried at 55 °C for 4 h. A drop of 2 mL distilled water was placed on the sample surface using a micrometric pipette at room temperature. The sample was immediately imaged, and the contact angle was measured automatically using a spherical fitting approach. Each contact angle reported herein is the mean of five independent measurements.

#### 2.4. Antimicrobial Test

The antimicrobial performance of a coating was evaluated according to the antimicrobial activity of a given coating surface against bacteria in contact with it. The antimicrobial test procedures were performed following the Japan Industrial Standard JIS Z 2801:2010 Antimicrobial products—Test for antimicrobial activity and efficacy, with minor modifications. Prior to the test, the plate samples were sterilized in a high-pressure steam autoclave operated at 121 °C, 103 kPa for 15 min, and then placed in sterile Petri dishes. The test bacteria used were *S. aureus* Gram-positive bacteria in suspension, adjusted at a cell concentration of  $5 \times 10^8$  colony-forming units per milliliter (cfu/mL). A 50  $\mu$ L suspension of the test bacteria was instilled onto the surface of a sample, and was then covered with a sterilized polyethylene film measuring 10 mm  $\times$  10 mm. The film was pressed so that the inoculum (test bacteria) spread evenly over the film, to avoid drop evaporation. An uncoated SS316L sample was used as a reference. Finally, the Petri dishes containing the inoculated test pieces were incubated at a temperature of 37 °C and a relative humidity of not less than 90% for 24 h.

After the inoculation, the test bacteria were washed out using 10 mL of phosphate-buffered saline. To conduct a viable cell count of bacteria, 10-fold serial dilutions and the agar plate culture method were used. Commercial Lysogeny broth agar was used (Difco Laboratories, Detroit, MI, USA). The incubation was performed at 37 °C for 24 h. After incubation, the number of visible bacterial colonies was counted using an agar plate in which 30 to 300 colonies appeared. To determine the antimicrobial performance, the following formula was used:

$$\text{Antibacterial Efficiency } (\eta) = (N_0 - N)/N_0 \times 100\%$$

where N (expressed in cfu) represents the number of viable cells of bacteria on the sample and  $N_0$  represents the number for the uncoated SS316L reference sample. The N value was calculated using  $C \cdot D$ , where C is an average of the number of colonies in three test pieces, and D is the corresponding dilution ratio of the diluted solution. The data presented herein were obtained from seven independent experiments.

The final condition of the bacterial colonies was imaged using a traditional camera. The statistical correlation of the antibacterial efficiency between the coated samples was determined using Student's *t*-test [34]. Differences were considered to be statistically significant when *p* was less than 0.01.

#### 2.5. Wear Test

The wear performance of the coatings was evaluated using a pin-on-disk rotating-sliding wear tester (Jun-Yan Precision Machine Co., Kaoshiung, Taiwan). The material of ball attached at the pin end was 100%  $\text{Al}_2\text{O}_3$ . The testing conditions were as follows: applied load, 10 N; line speed, 0.2 m/s; rotating radius, 6 mm; and sliding distance, 350 m. The resulting wear track was measured by scanning four cross-sections at an interval of 90° using a white-light interferometer (BMT, Nuremberg, Germany). The wear rate was calculated by the formula  $2\pi RA/WL$ , where R is the rotating radius, A is an average of four measurements of a wear cross area, W is the load, and L is the sliding distance.

### 3. Results and Discussion

#### 3.1. Coatings

Figure 1 shows the binding energy of the CN<sub>x</sub> coating characterized by XPS. Figure 1a provides the C1s core-level XPS spectrum. A major peak was observed at 284.8 eV, with a minor protrusion at 285.9 eV, which could be deconvoluted into two components with the broader peak corresponding to (C, N) bonding and the other peak corresponding to a-C. The eV values of C-N (286.3 eV) and C = N (285.5 eV) peaks are close and mostly overlap each other [35,36]. The deconvolution of the C-N/C = N peak is un-meaningful [37]. It can be concluded that the (C, N) peak was composed of C-N and C = N peaks. The spectrum of a-C phase at 284.5 eV covered a wide range of 283–287 eV, suggesting

the formation of  $sp^2$  a-C (284.2 eV) [38] and  $sp^3$  a-C (284.9 eV) [39]. The presence of a-C structures in the CN<sub>x</sub> coating was further confirmed by the Raman spectroscopy analysis results, as listed in Table 2. Raman spectroscopy is a highly effective method for characterizing the detailed bonding structure of carbon nanomaterials. When the ID/IG value is >1, a-C is present, including  $sp^2$  a-C and  $sp^3$  a-C. With a higher ID/IG value, the material is more amorphous. The data in Table 2 indicate that metal doping led to an increase in amorphization. For the CN<sub>x</sub> coating, the ID/IG value was 1.49, which indicates the presence of a-C. Figure 1b shows the N1s core-level XPS spectrum. The raw CN<sub>x</sub> peak could be deconvoluted into two components corresponding to a N-C peak at 398.3 eV and a N = C peak at 400.2 eV [40]. Figure 1b and the ID/IG value indicate that the CN<sub>x</sub> coating was a mixture of CN<sub>x</sub> and a-C phases.

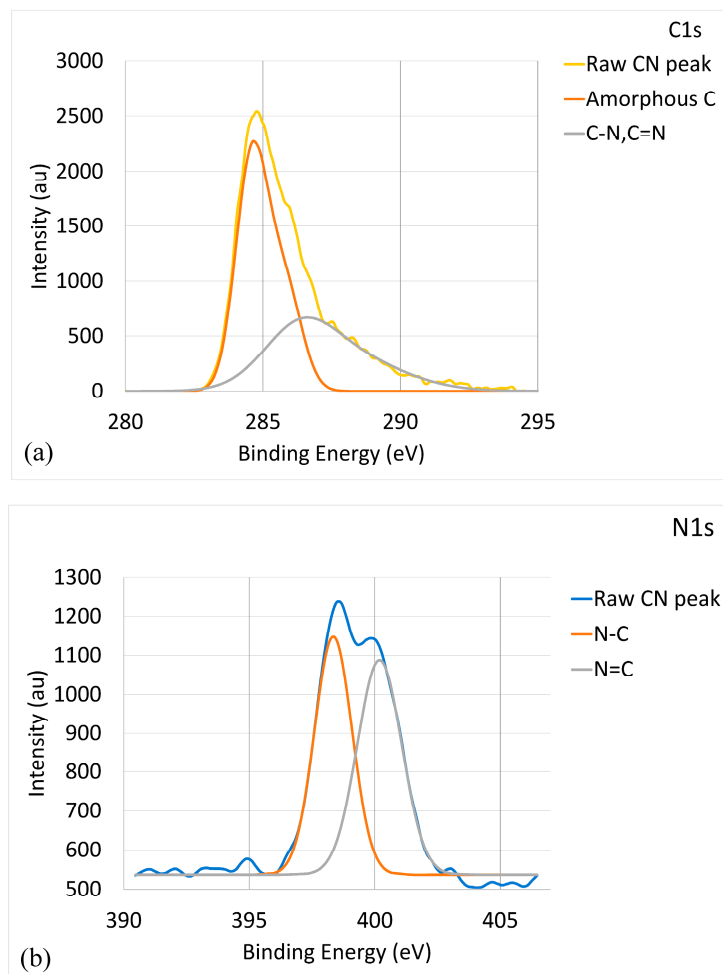


**Figure 1.** Bonding energy of CN<sub>x</sub> coating characterized by XPS: (a) C1s XPS raw and deconvoluted spectra; and (b) N1s XPS raw and deconvoluted spectra.

Figure 2 illustrates the bonding energy of CN<sub>x</sub>-Zr coating characterized by XPS. Figure 2a provides the C1s core-level XPS spectrum. The deconvolution produced similar results to Figure 1a, but with a lower strength for the (C, N) peak. The C-Zr peak was very weak and could not be distinguished with certainty. The ID/IG value was 2.85, indicating the presence of a-C. Figure 2b shows the N1s core-level XPS spectrum. The broad peak could be deconvoluted into three components corresponding to a major N-C peak at 398.2 eV, a N = C peak at 400.1 eV, and a N-Zr peak at 397.1 eV [40,41]. Figure 2c presents the Zr3d core-level XPS spectrum. The deconvolution indicated a major Zr-C peak at 182.9 eV, a Zr-N peak at 185.1 eV, and a Zr-O peak at 181.5 eV [42]. The presence of Zr-O was caused by the

improper storage of the sample prior to performing the XPS analyses. Therefore, the result reveals that the CN<sub>x</sub>-Zr coating comprised a-C, CN<sub>x</sub>, and ZrC/ZrN phases.

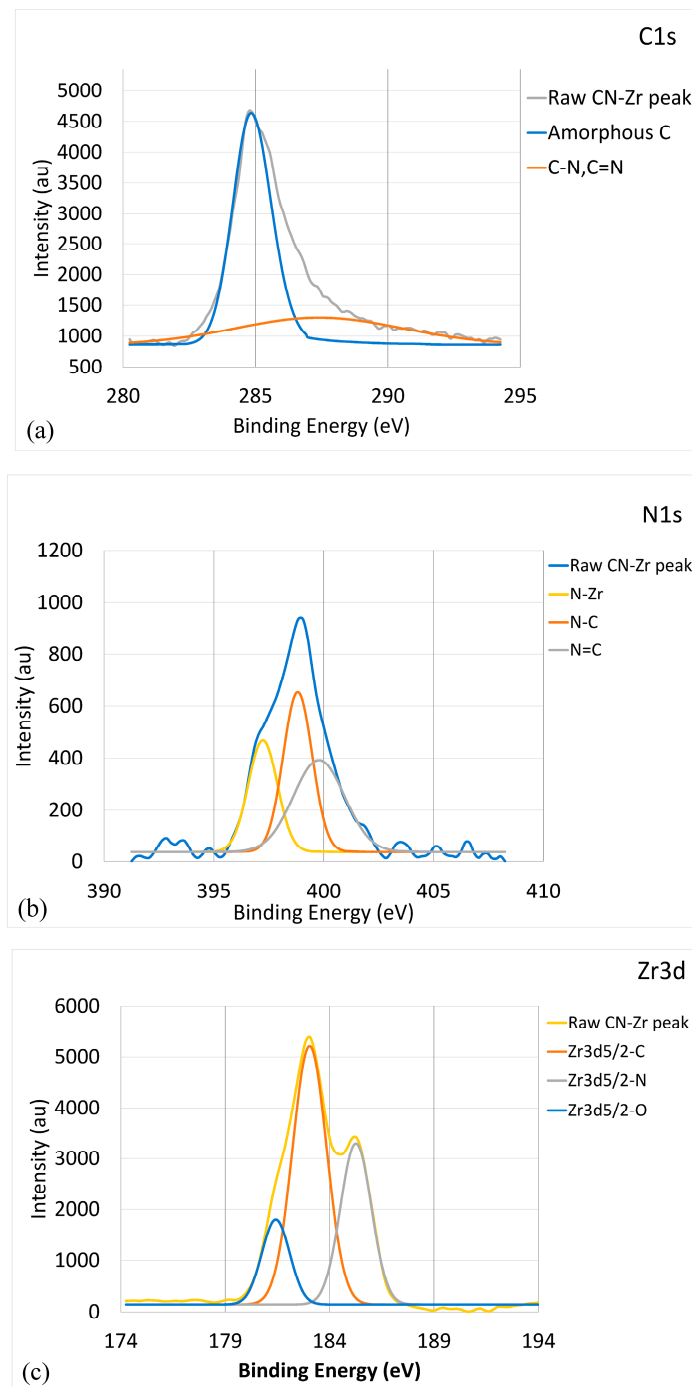


**Figure 2.** Bonding energy of CN<sub>x</sub>-Zr coating characterized by XPS: (a) C1s XPS raw and deconvoluted spectra; (b) N1s XPS raw and deconvoluted spectra; and (c) Zr3d raw and deconvoluted spectra.

The analyses of XPS spectra of the CN<sub>x</sub>-W coating showed that it was a mixture of a-C, CN<sub>x</sub>, and WC/WN phases. Similarly, the CN<sub>x</sub>-Cr coating consisted of a-C, CN<sub>x</sub>, and CrC/CrN phases. However, the CN<sub>x</sub>-Ti coating differed, as illustrated in Figure 3. Figure 3a shows the C1s core-level XPS spectrum. The deconvoluted peaks included an a-C peak and a C-N peak; the C-Ti peak (281.7 eV) [43] nearly approached zero. This indicates that TiC was present in minute amounts,

or absent. As shown in Figure 3b, the deconvolution of the N1s core-level XPS spectrum included a major N-C peak, a N = C peak, and a N-Ti peak (397 eV) [41]. Figure 3c provides the Ti2p core-level XPS spectrum, in which, after deconvolution, two Ti-N peaks (455.8 and 460.9 eV [44]) and two Ti-O peaks (454.6 and 464.7 eV [45]) could be obtained. Improper storage of the sample before performing the XPS analyses resulted in the appearance of Ti-O. No Ti-C bonding was detected. Therefore, the CN<sub>x</sub>-Ti coating was a mixture of a-C, CN<sub>x</sub>, and TiN phases; no TiC phase was grown.

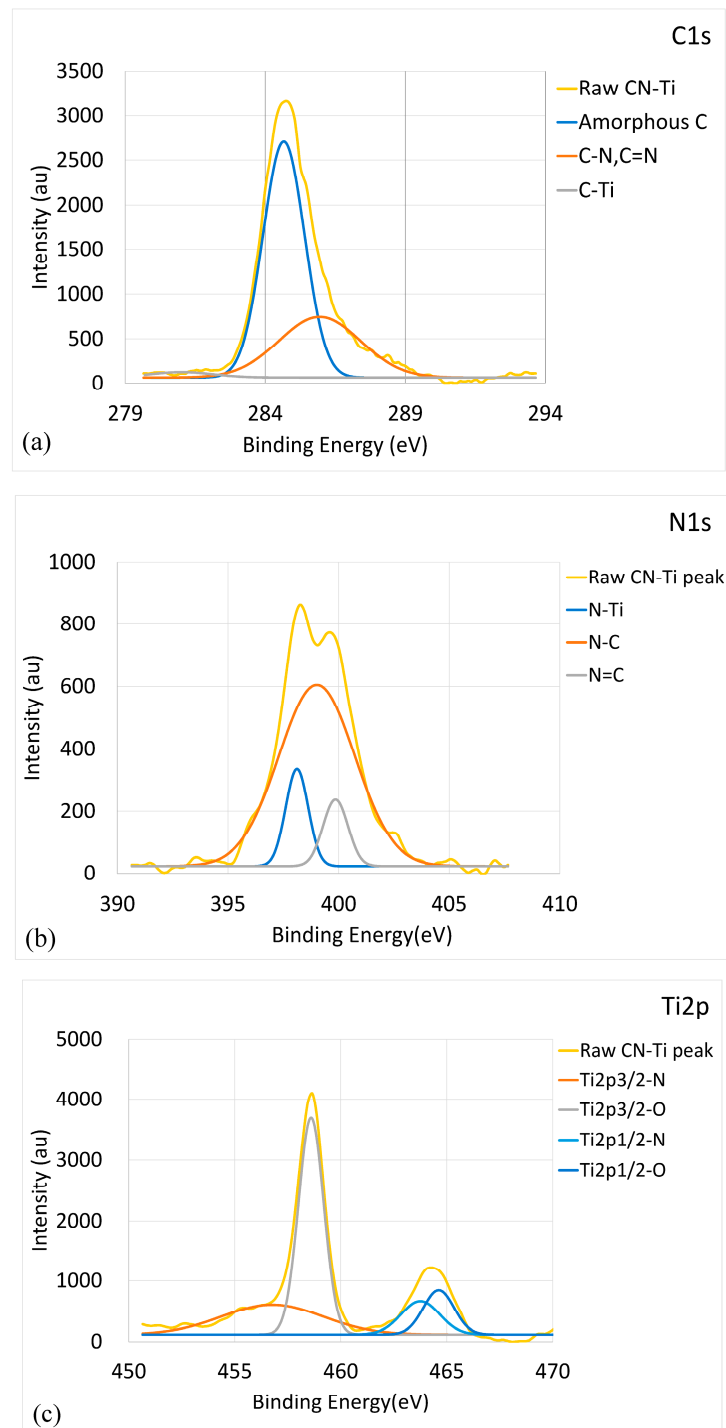


**Figure 3.** Bonding energy of CN<sub>x</sub>-Ti coating characterized by XPS: (a) C1s XPS raw and deconvoluted spectra; (b) N1s XPS raw and the deconvoluted spectra; and (c) Ti2p raw and deconvoluted spectra.

When the bonding concentration of C and N was derived from the doped metals' core-level XPS spectrum, the binding states of carbide and nitride could be compared. As presented in Figure 2c, the content of Zr-C bonding was higher than that of Zr-N; the same was true for Cr-C and Cr-N. Comparatively, as shown in Figure 4, the content of W-N bonding was higher than that of W-C bonding in the CN<sub>x</sub>-W coating. These results demonstrate the different tendencies of each metal to form C or N compounds.

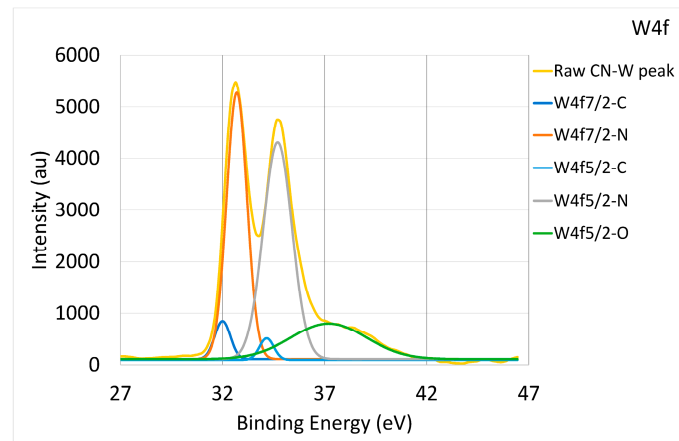


**Figure 4.** W4f XPS raw and deconvoluted spectra derived from bonding energy of CN<sub>x</sub>-W coating characterized by XPS.

Typical X-ray diffraction (XRD) spectra for the CN<sub>x</sub> and 6 at. % metal-doped CN<sub>x</sub> coatings are shown in Figure 5. For the CN<sub>x</sub> coating, no obvious crystalline peak was evident, indicating the presence of an amorphous CN<sub>x</sub> (a-CN<sub>x</sub>) structure. Thus, the results of XRD, XPS (Figure 1), and Raman analyses (Table 2) indicated that the CN<sub>x</sub> coating was a composite containing a-CN<sub>x</sub> and a-C structures. Under the applied conditions, pure a-CN<sub>x</sub> could not be obtained. For simplicity, the term “CN<sub>x</sub>” is used in the following. For the other metal-doped coatings, crystalline phases were evident. For the CN<sub>x</sub>-Ti coating, the results of XRD, XPS, and Raman analyses indicated that the CN<sub>x</sub> coating functioned as a matrix, with the crystalline TiN phase dispersed in it. The lack of formation of the TiC phase was also confirmed. For the other doped CN<sub>x</sub> coatings, different types of carbides and nitrides were present. The results of XRD, XPS, and Raman analyses indicated that the CN<sub>x</sub>-W coating was a composite comprising crystalline W<sub>2</sub>N and WC phases dispersed within the CN<sub>x</sub> coating. The CN<sub>x</sub>-Cr and CN<sub>x</sub>-Zr coatings had crystalline CrN/CrC phases and Zr<sub>2</sub>N/ZrC phases, respectively, which were dispersed within the CN<sub>x</sub> coating.

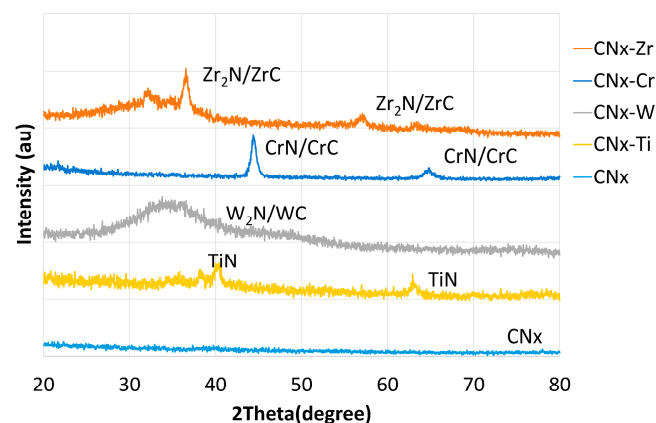


**Figure 5.** XRD patterns of CN<sub>x</sub> and 6 at. % metal-doped CN<sub>x</sub> coatings.

Figure 6 provides a comparison of the coatings with respect to their hardness and hardness-to-elastic modulus ratio (H/E). The CN<sub>x</sub> coating exhibited the highest values. Metal doping reduced the hardness values. These results indicate that the metal-doped CN<sub>x</sub> coatings consisted of a CN<sub>x</sub> coating with carbide/nitride compound(s) dispersed throughout. These compound(s) impaired the overall integrity of the coatings. Thus, the hardness of the metal-doped CN<sub>x</sub> coatings was lower than that of the CN<sub>x</sub> coating. Moreover, the different types of nitride/carbide compounds formed and their dispersed states and the a-CN<sub>x</sub>/a-C ratio also affected the hardness. The hardness of the metal-doped coatings, ranked in descending order, was CN<sub>x</sub>-W > CN<sub>x</sub>-Ti > CN<sub>x</sub>-Zr > CN<sub>x</sub>-Cr. When a nanohardness tester is used, the Young's modulus can be measured simultaneously. The H/E values were calculated, and their order, ranked in descending order, was CN<sub>x</sub>-Ti > CN<sub>x</sub>-W > CN<sub>x</sub>-Cr > CN<sub>x</sub>-Zr.

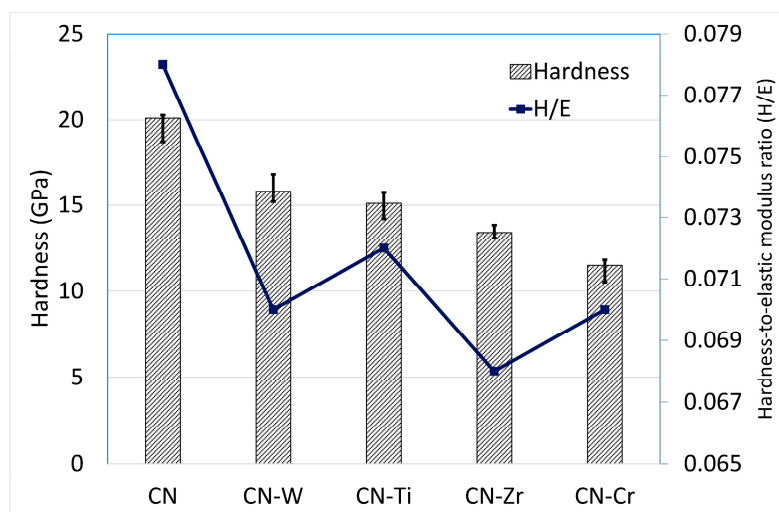


**Figure 6.** Hardness and hardness-to-elastic modulus ratio (H/E) values of CN<sub>x</sub> and 6 at. % metal-doped CN<sub>x</sub> coatings.

The average surface roughness (Ra) of the CN<sub>x</sub> coating was very low, at 31 nm (Table 2). Metal doping caused the Ra values to be reduced by 50–70%, as a result of the increase in amorphization. All the coatings exhibited comparable adhesion values, ranging from 68 N to 80 N.

**Table 2.** Surface roughness, adhesion and ID/IG values (Raman analyses) of CN<sub>x</sub> and 6 at. % metal-doped CN<sub>x</sub> coatings.

| Samples             | Surface Roughness Ra (nm) | Adhesion <i>L<sub>c</sub></i> (N) | ID/IG |
|---------------------|---------------------------|-----------------------------------|-------|
| CN <sub>x</sub>     | 31                        | 68                                | 1.49  |
| CN <sub>x</sub> -W  | 12                        | 68                                | 1.63  |
| CN <sub>x</sub> -Ti | 10                        | 74                                | 2.10  |
| CN <sub>x</sub> -Zr | 17                        | 80                                | 2.85  |
| CN <sub>x</sub> -Cr | 18                        | 75                                | 1.72  |

### 3.2. Hydrophilicity Test

The hydrophilicity of a surface is an important factor when studying the viability of bacteria. Typically, the higher the hydrophilicity (lower wettability) of a surface is, the higher the contact angle and its antibacterial performance are [46]. Hydrophilicity is influenced by surface properties such as chemical characteristics and morphology.

The results of the hydrophilicity test for the uncoated and coated samples are illustrated in Figure 7. The CN<sub>x</sub> coating exhibited a slightly higher angle than the uncoated SS316L sample. The CN<sub>x</sub>-Ti, CN<sub>x</sub>-Zr, and CN<sub>x</sub>-Cr coatings displayed further increases in their contact angles. However, the angle

of the CNx-W coating was lower than that of the uncoated SS316L sample, despite the CNx-W coating having very low surface roughness (Table 2). The CNx-Zr coating, which had a medium-level Ra value, exhibited the highest contact angle. Thus, for these coated samples, the surface morphology was not the main factor affecting the contact angle. Chemical characteristics may be the main cause because each coating had a different composition and constituent phases.

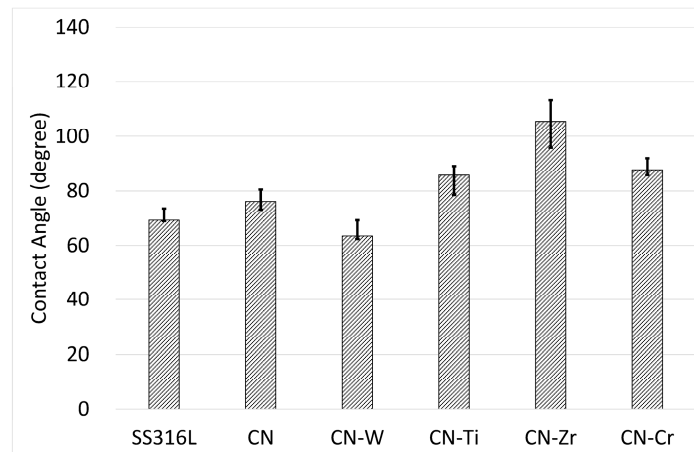


**Figure 7.** Contact angle values of uncoated SS316L and CNx- and 6 at. % metal-doped CNx-coated samples.

### 3.3. Antimicrobial Test

*S. aureus* and *A. actinomycetemcomitans* are considered common causes of postoperative infection and inflammatory reactions [47,48], which begin with bacterial colonization of implants or tissue surfaces. Biomaterials and medical tools with antibacterial surfaces may help to reduce the formation of bacterial colonies and thereby avoid inflammation.

In the present study, *S. aureus* was incubated on the surfaces of uncoated SS316L and CNx- and 6 at. % metal-doped CNx-coated plates to evaluate their antimicrobial performance. By applying the uncoated SS316L sample as a reference, we could obtain the *antibacterial efficiency* ( $\eta$ ) values (Figure 8). The results revealed that  $\eta = 25\%$  for the CNx coating, indicating that the CNx coating reduced the bacterial count of inoculum by 25% relative to the uncoated SS316L plate. These experimental results indicate that all the coatings showed antibacterial ability. The CNx-Zr coating displayed the highest antimicrobial performance and had a substantially higher  $\eta$  value than the single CNx coating. Second most effective was the CNx-Cr coating, followed by the CNx-W coating. However, the CNx-Ti coating exhibited markedly lower antibacterial performance than the CNx coating.

Figure 9 depicts typical photographs of bacterial colonies on the agar plates after incubation for 24 h on the uncoated SS316L (Figure 9a) and CNx-Zr coated (Figure 9b) samples. The antimicrobial performance of the CNx-Zr coatings was very pronounced. These results confirm that the numbers of viable bacteria were lower on the CNx and 6 at. % metal-doped CNx coatings than on the uncoated SS316L reference sample.

The antibacterial ability of the coatings appeared to be related to hydrophilicity. The CNx-Zr and CNx-Cr coatings, which exhibited high hydrophilicity, displayed excellent antibacterial performance. However, this relation did not apply to the other coatings. The CNx-Ti coating, which had a highly hydrophilic surface, showed the lowest antibacterial ability. Some researchers reported that C aggregates combat microorganisms by physically damaging the outer membranes of cells [49]. This can explain the increase in antibacterial performance of the coatings in the current study, because all the coatings were carbon-based. However, the coatings also contained N, and N-C bonding was detected. In addition, the coatings contained metal carbides/nitrides. To date, no related data have been reported.

Based on these interaction effects, the causes of the different antimicrobial performance levels are complex and need further investigation.

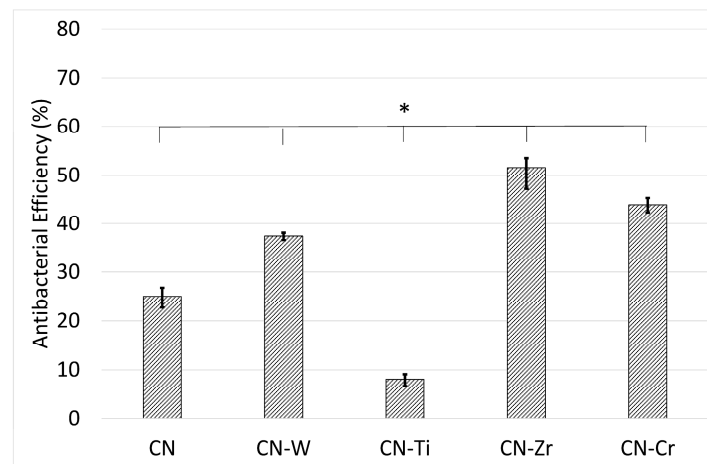


**Figure 8.** Antibacterial efficiency ( $\eta$ ) evaluated using *Staphylococcus aureus* on CNx- and 6 at. % metal-doped CNx-coated SS316L samples, with the uncoated SS316L ones serving as a reference. (\*) A value of  $p < 0.01$  was considered to indicate a significant difference between the values of the two groups of samples.

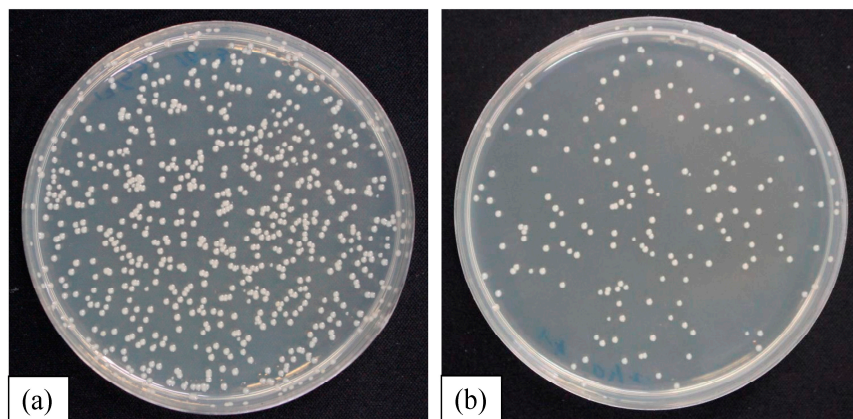


**Figure 9.** Typical photographs of visualized colonies on the agar plates after incubation for 24 h on (a) uncoated SS316L; and (b) CNx-Zr coated samples.

### 3.4. Wear Test

The results of the wear test are illustrated in Figure 10. The data for the uncoated SS316L sample are not included due to its very high value, which was twice that of the CNx coating. The CNx coating showed the lowest wear resistance, whereas metal doping greatly improved wear resistance. The CNx-W and CNx-Ti coatings displayed the highest wear resistance and were comparable to each other. Second was the CNx-Zr coating. Finally, the CNx-Cr coating exhibited the lowest wear resistance. Regarding the detected friction coefficient, there was no direct relationship with wear behavior.

Figure 6 presents the H/E values. A rule proposed by Affonso [50] is commonly used to predict the wear resistance of materials, either in bulk or coating form, by using H/E values. The higher the H/E value is, the higher the wear resistance. Here, this rule cannot be effectively applied. By comparing the wear rate in Figure 10 and coating hardness in Figure 6, we could obtain a relationship for the four metal-doped coatings. The wear resistance followed the same trend as that of the hardness values. That is, coatings with higher hardness showed lower wear rates. Therefore, the wear resistance

of the materials had the order  $CN_x-W \approx CN_x-Ti > CN_x-Zr > CN_x-Cr$ , following the trend of the hardness values.

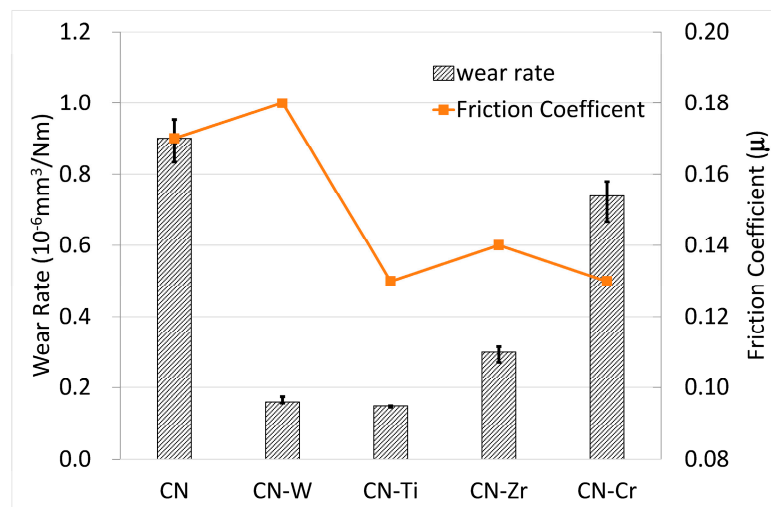


**Figure 10.** Comparison of wear test results of  $CN_x$  and 6 at. % metal-doped  $CN_x$  coated samples

#### 4. Conclusions

SS316L materials have been widely applied in the field of biomaterials and medical tools. However, it shows relatively low wear resistance. In this study, we prepared  $CN_x$  and 6 at. % metal-doped  $CN_x$  coatings on SS316L substrates by using an industrial-scale four-target closed-field unbalanced DC magnetron sputtering system. The metals used were W, Ti, Zr, and Cr. The coatings were characterized and studied for antimicrobial and wear performance. Under the applied conditions, the  $CN_x$  coating was found to be a composite containing  $\alpha$ - $CN_x$  and  $\alpha$ -C structures. For the metal-doped coatings, the metal reacted with C/N to form crystalline carbides/nitrides that were dispersed in the  $CN_x$  coatings. Metal doping reduced the hardness and surface roughness. No substantial difference in adhesion was observed between coatings. All the coatings, both  $CN_x$  and metal-doped  $CN_x$ , exhibited antimicrobial ability relative to the uncoated SS316L sample. Of the doped coatings, the  $CN_x$ -Zr coating showed low surface roughness and the highest hydrophilicity. The  $CN_x$ -Zr coated sample displayed excellent antibacterial performance, despite having slightly lower wear performance. The favorable results for the  $CN_x$ -Zr coating are very encouraging due to the high biocompatibility of C, N, and Zr elements. The  $CN_x$ -Zr coating merits further study.

**Author Contributions:** S.H.Y. and Y.L.S. conceived and designed the experiments; Y.C.L. performed the experiments; S.H.Y., Y.L.S. and Y.C.L. analyzed the data; S.H.Y. and Y.C.L. contributed reagents/materials/analysis tools; S.H.Y. wrote the paper.

**Conflicts of Interest:** The authors declare no conflict of interest.

#### References

- Muzio, G.; Miola, M.; Perero, S.; Oraldi, M.; Maggiora, M.; Ferraris, S.; Vernè, E.; Festa, V.; Festa, F.; Canuto, R.A.; et al. Polypropylene prostheses coated with silver nanoclusters/silica coating obtained by sputtering: Biocompatibility and antibacterial properties. *Surf. Coat. Technol.* **2017**, *319*, 326–334. [[CrossRef](#)]
- Etiemble, A.; Der Loughian, C.; Apreutesei, M.; Langlois, C.; Cardinal, S.; Pelletier, J.M.; Pierson, J.-F.; Steyer, P. Innovative Zr-Cu-Ag thin film metallic glass deposited by magnetron PVD sputtering for antibacterial applications. *J. Alloys Compd.* **2017**, *707*, 155–161. [[CrossRef](#)]
- Groessner-Schreiber, B.; Herzog, M.; Hedderich, J.; Duck, A.; Hannig, M.; Griepentrog, M. Focal adhesion contact formation by fibroblasts cultured on surface-modified dental implants: An in vitro study. *Clin. Oral Implants Res.* **2006**, *17*, 736–745. [[CrossRef](#)] [[PubMed](#)]

4. Groessner-Schreiber, B.; Hannig, M.; Dück, A.; Griepentrog, M.; Wenderoth, D.F. Do different implant surfaces exposed in the oral cavity of humans show different biofilm compositions and activities? *Eur. J. Oral Sci.* **2004**, *112*, 516–522. [[CrossRef](#)] [[PubMed](#)]
5. Huang, H.L.; Chang, Y.Y.; Lai, M.C.; Lin, C.R.; Lai, C.H.; Shieh, T.M. Antibacterial TaN-Ag coatings on titanium dental implants. *Surf. Coat. Technol.* **2010**, *205*, 1636–1641. [[CrossRef](#)]
6. Nuñez, J.A.P.; Salapare, H.S.; Villamayor, M.M.S.; Siringan, M.A.T.; Ramos, H.J. Enhanced adsorption of Ag<sup>+</sup> on triethanolamine modified titanate nanotubes. *Surf. Interfaces* **2017**, *8*, 28–35. [[CrossRef](#)]
7. Marciano, F.R.; Bonetti, L.F.; Mangolin, J.F.; Da-Silva, N.S.; Corat, E.J.; Trava-Airoldi, V.J. Investigation into the antibacterial property and bacterial adhesion of diamond-like carbon films. *Vacuum* **2011**, *85*, 662–666. [[CrossRef](#)]
8. Zhou, H.; Xu, L.; Ogino, A.; Nagatsu, M. Investigation into the antibacterial property of carbon films. *Diam. Relat. Mater.* **2008**, *17*, 1416–1419. [[CrossRef](#)]
9. Jeyachandran, Y.L.; Venkatachalam, S.; Karunakaran, B.; Narayandass, S.K.; Mangalaraj, D.; Bao, C.Y.; Zhang, C.L. Enhanced ionodetection by using polyethyleneimine as an insulator material. *Mater. Sci. Eng. C* **2007**, *27*, 35–41. [[CrossRef](#)]
10. Hilbert, L.R.; Bagge-Ravn, D.; Kold, J.; Gram, L. Influence of surface roughness of stainless steel on microbial adhesion and corrosion resistance. *Int. Biodeterior. Biodegrad.* **2003**, *52*, 175–185. [[CrossRef](#)]
11. Marciano, F.R.; Bonetti, L.F.; Da-Silva, N.S.; Corat, E.J.; Trava-Airoldi, V.J. Wettability and antibacterial activity of modified diamond-like carbon films. *Appl. Surf. Sci.* **2009**, *255*, 8377–8382. [[CrossRef](#)]
12. Ishihara, M.; Kosaka, T.; Nakamura, T.; Tsugawa, K.; Hasegawa, M.; Kokai, F.; Koga, Y. Antibacterial activity of DLC and Ag–DLC films produced by PECVD technique. *Diam. Relat. Mater.* **2006**, *15*, 1010–1014.
13. Liu, A.Y.; Cohen, M.L. Prediction of new low compressibility solids. *Science* **1989**, *245*, 841–842. [[CrossRef](#)] [[PubMed](#)]
14. Wäsche, R.; Hartelt, M.; Springborn, U.; Bewilogua, K.; Keunecke, M. Wear of carbon nitride coatings under oscillating sliding conditions. *Wear* **2010**, *269*, 816–825. [[CrossRef](#)]
15. Takadoun, J.; Rauch, J.Y.; Cattenot, J.M.; Martin, N. Comparative study of mechanical and tribological properties of CN and x DLC films deposited by PECVD technique. *Surf. Coat. Technol.* **2003**, *174*, 427–433. [[CrossRef](#)]
16. Park, Y.S.; Myung, H.S.; Han, J.G. Characterization of CN<sub>x</sub> thin films prepared by close field unbalanced magnetron sputtering. *Thin Solid Films* **2005**, *475*, 298–302. [[CrossRef](#)]
17. Camero, M.; Buijnsters, J.G.; Gómez-Alexandre, C.; Gago, R.; Caretti, I.; Jiménez, I. The effect of nitrogen incorporation on the bonding structure of hydrogenated carbon nitride films. *J. Appl. Phys.* **2007**, *101*, 063515. [[CrossRef](#)]
18. Zhang, S.; Fu, Y.; Du, H.; Zeng, X.T.; Liu, Y.C. Magnetron sputtering of nanocomposite (Ti,Cr)CN/DLC coatings. *Surf. Coat. Technol.* **2002**, *162*, 42–48. [[CrossRef](#)]
19. Hsu, C. Effects of Tungsten Addition on Mechanical and Tribological Properties of Carbon Nitride Prepared by DC Magnetron Sputtering. Master's Thesis, National Cheng Kung University, Tainan, Taiwan, 2014.
20. Wu, X. Effect of Chromium Addition on Tribological Properties and Corrosion Resistance of Carbon Nitride Prepared by DC Magnetron Sputtering. Master's Thesis, National Cheng Kung University, Tainan, Taiwan, 2015.
21. Yeh, K. Effect of Titanium Addition on Mechanical and Tribological Properties of Carbon Nitride (a-CN<sub>x</sub>) Prepared by DC Magnetron Sputtering. Master's Thesis, National Cheng Kung University, Tainan, Taiwan, 2016.
22. Lai, C.-H.; Chang, Y.-Y.; Huang, H.-L.; Kao, H.-Y. Characterization and antibacterial performance of ZrCN/amorphous carbon coatings deposited on titanium implants. *Thin Solid Films* **2011**, *520*, 1525–1531. [[CrossRef](#)]
23. Huang, H.-L.; Chang, Y.-Y.; Liu, J.-X.; Tsai, M.-T.; Lai, C.-H. Antibacterial activity and cell compatibility of TiZrN, TiZrCN, and TiZr-amorphous carbon coatings. *Thin Solid Films* **2015**, *596*, 111–117. [[CrossRef](#)]
24. Hosokawa, A.; Shimamura, K.; Ueda, T. Cutting characteristics of PVD-coated tools deposited by unbalanced magnetron sputtering method. *CIRP Ann. Manuf. Technol.* **2012**, *61*, 95–98. [[CrossRef](#)]
25. Kuptsov, K.A.; Kiryukhantsev-Korneev, P.V.; Sheveyko, A.N.; Shtansky, D.V. Effect of laser shock peening on microstructure, mechanical properties and corrosion behavior of interstitial free steel. *Surf. Coat. Technol.* **2013**, *216*, 273–281. [[CrossRef](#)]

26. Polcara, T.; Vitu, T.; Cvrcek, L.; Vyskocil, J.; Cavaleiro, A. Effects of carbon content on the high temperature friction and wear of chromium carbonitride coatings. *Tribol. Int.* **2010**, *43*, 1228–1233. [[CrossRef](#)]
27. Cotrut, C.; Braic, V.; Balaceanu, M.; Titorencu, I.; Braic, M.; Parau, A.C. Corrosion resistance, mechanical properties and biocompatibility of Hf-containing ZrCN coatings. *Thin Solid Films* **2013**, *538*, 48–55. [[CrossRef](#)]
28. Wang, L.; Zhao, X.; Ding, M.H.; Zheng, H.; Zhang, H.S.; Zhang, B.; Li, X.Q.; Wu, G.Y. Surface modification of biomedical AISI 316L stainless steel with zirconium carbonitride coatings. *Appl. Surf. Sci.* **2015**, *340*, 113–119. [[CrossRef](#)]
29. Grigore, E.; Ruset, C.; Li, X.; Dong, H. Zirconium carbonitride films deposited by combined magnetron sputtering and ion implantation (CMSII). *Surf. Coat. Technol.* **2010**, *204*, 1889–1892. [[CrossRef](#)]
30. Yao, S.H.; Su, Y.L.; Kao, W.H.; Cheng, K.W. Wear behavior of DC unbalanced magnetron sputter deposited ZrCN films. *Mater. Lett.* **2005**, *59*, 3230–3233. [[CrossRef](#)]
31. Ospina, R.; Escobar, D.; Restrepo-Parra, E.; Arango, P.J.; Jurado, J.F. Mechanical and tribological behavior of W/WCN bilayers grown by pulsed vacuum arc discharge. *Tribol. Int.* **2013**, *62*, 124–129. [[CrossRef](#)]
32. Chen, X.; Peng, Z.; Fu, Z.; Wu, S.; Yue, W.; Wang, C. Microstructural, mechanical and tribological properties of tungsten-gradually doped diamond-like carbon films with functionally graded interlayers. *Surf. Coat. Technol.* **2011**, *205*, 3631–3638. [[CrossRef](#)]
33. Shirley, D.A. High-resolution X-ray photoemission spectrum of the valence bands of gold. *Phys. Rev. B* **1972**, *5*, 4709–4716. [[CrossRef](#)]
34. Srivastava, M.S. *Methods of Multivariate Statistics*; Wiley-Interscience: New York, NY, USA, 2004; p. 109.
35. Yu, W.; Ren, G.B.; Wang, S.F.; Han, L.; Li, X.W.; Zhang, L.S.; Fu, G.S. Effect of gas pressure on the synthesis of carbon nitride films during plasma-enhanced chemical vapor deposition. *Thin Solid Films* **2002**, *402*, 55–59. [[CrossRef](#)]
36. Zocco, A.; Perrone, A.; Broitman, E.; Czigany, Z.; Hultman, L.; Anderle, M.; Laidani, N. Mechanical and tribological properties of CN<sub>x</sub> films deposited by reactive pulsed laser ablation. *Diam. Relat. Mater.* **2002**, *11*, 98–104. [[CrossRef](#)]
37. Permatasari, F.A.; Aimon, A.H.; Iskandar, F.; Ogi, T.; Okuyama, K. Role of C–N configurations in the photoluminescence of graphene quantum dots synthesized by a hydrothermal route. *Sci. Rep.* **2016**, *6*, 21042. [[CrossRef](#)] [[PubMed](#)]
38. Chang, Y.Y.; Wang, D.Y.; Wu, W. Catalysis effect of metal doping on wear properties of diamond-like carbon films deposited by a cathodic-arc activated deposition process. *Thin Solid Films* **2002**, *420*, 241–247. [[CrossRef](#)]
39. Zheng, Y.; Liu, X.; Zhang, H. Properties of Zr–ZrC–ZrC/DLC gradient films on TiNi alloy by the PIIID technique combined with PECVD. *Surf. Coat. Technol.* **2008**, *202*, 3011–3016. [[CrossRef](#)]
40. Xu, J.; Wang, Y.; Shang, J.; Ma, D.; Li, Y. Preparation of mesoporous carbon nitride materials using urea and formaldehyde as precursors and catalytic application as solid bases. *Appl. Catal. A Gen.* **2017**, *538*, 221–229. [[CrossRef](#)]
41. Badrinarayanan, S.; Sinha, S.; Mandale, A.B. XPS studies of nitrogen ion implanted zirconium and titanium. *J. Electron Spectrosc. Relat. Phenom.* **1989**, *49*, 303–309. [[CrossRef](#)]
42. Anderson, J.A.; Fierro, J.L.G. Bulk and surface properties of copper-containing oxides of the general formula LaZr<sub>1-x</sub>Cu<sub>x</sub>O<sub>3</sub>. *J. Solid State Chem.* **1994**, *108*, 305–313. [[CrossRef](#)]
43. Galuska, A.A.; Uht, J.C.; Marquez, N. Reactive and nonreactive ion mixing of Ti films on carbon substrates. *J. Vac. Sci. Tech. A* **1988**, *6*, 110–122. [[CrossRef](#)]
44. Chourasia, A.R.; Chopra, D.R. X-ray photoelectron spectra of TiN. *Surf. Sci. Spectra* **1992**, *1*, 233–237. [[CrossRef](#)]
45. Saied, S.O.; Sullivan, J.L.; Choudhury, T.; Pearce, C.G. A comparison of ion and fast atom beam reduction in TiO<sub>2</sub>. *Vacuum* **1988**, *38*, 917–922. [[CrossRef](#)]
46. Chang, Y.-Y.; Huang, H.-L.; Chen, H.-J.; Lai, C.-H.; Wen, C.-Y. Antibacterial properties and cytocompatibility of tantalum oxide coatings. *Surf. Coat. Technol.* **2014**, *259*, 193–198. [[CrossRef](#)]
47. Harris, L.G.; Richards, R.G. Staphylococci and implant surfaces: A review. *Injury* **2006**, *37*, S3–S14. [[CrossRef](#)] [[PubMed](#)]
48. Van Winkelhoff, A.; Wolf, J. Actinobacillus actinomycetemcomitans-associated peri-implantitis in an edentulous patient. *J. Clin. Periodontol.* **2000**, *27*, 531–535. [[CrossRef](#)] [[PubMed](#)]

49. Kang, S.; Pinault, M.; Pfefferle, L.D.; Elimelech, M. Single-walled carbon nanotubes exhibit strong antimicrobial activity. *Langmuir* **2007**, *23*, 8670–8673. [[CrossRef](#)] [[PubMed](#)]
50. Affonso, L.O. *Machinery Failure Analysis Handbook—Sustain Your Operations and Maximize Uptime*; Gulf Publishing Company: Houston, TX, USA, 2006.



© 2017 by the authors. Licensee MDPI, Basel, Switzerland. This article is an open access article distributed under the terms and conditions of the Creative Commons Attribution (CC BY) license (<http://creativecommons.org/licenses/by/4.0/>).